

Gallium Composition-Dependent Structural Phase Transitions in $\text{HoFe}_{3-x}\text{Ga}_x(\text{BO}_3)_4$ Solid Solutions: Crystal Growth, Structure, and Raman Spectroscopy Study

Evgeniya Moshkina, Svetlana Krylova,* Irina Gudim, Maxim Molochev, Vladislav Temerov, M. S. Pavlovskiy, Alexander Vtyurin, and Alexander Krylov



Cite This: *Cryst. Growth Des.* 2020, 20, 1058–1069



Read Online

ACCESS |



Metrics & More

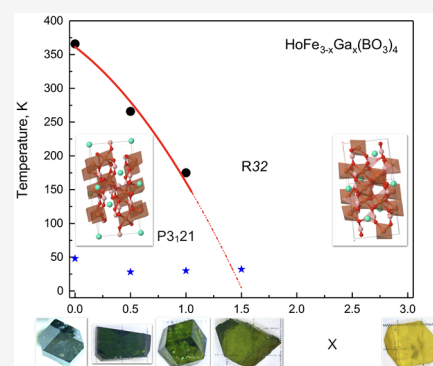


Article Recommendations



Supporting Information

ABSTRACT: Single crystals of solid solutions of $\text{HoFe}_{3-x}\text{Ga}_x(\text{BO}_3)_4$ with $x = 0, 0.5, 1, 1.5,$ and 3 were obtained using flux synthesis. The conditions of the synthesis are described in detail. The structural properties of each of the synthesized samples were studied using X-ray powder diffraction analysis at several temperature points (303, 403, and 503 K). The structural parameters of the obtained samples and the “pure” compounds $\text{HoFe}_3(\text{BO}_3)_4$ and $\text{HoGa}_3(\text{BO}_3)_4$ were compared. The Raman spectra of the obtained solid solutions $\text{HoFe}_{3-x}\text{Ga}_x(\text{BO}_3)_4$ were studied in a wide temperature range ($T = 10\text{--}400$ K). The vibrational spectra and eigenvectors of the $\text{HoFe}_3\text{Ga}(\text{BO}_3)_4$ and $\text{HoGa}_3(\text{BO}_3)_4$ in R32 phase and $\text{HoFe}_3\text{Ga}(\text{BO}_3)_4$ in P3₁21 phase were calculated within density functional theory. The features of the Raman spectra of $\text{HoFe}_2\text{Ga}(\text{BO}_3)_4$, $\text{HoFe}_{2.5}\text{Ga}_{0.5}(\text{BO}_3)_4$, $\text{HoFe}_3(\text{BO}_3)_4$ crystals associated with the R32 \rightarrow P3₁21 structural phase transition, which have a strong dependence on the degree of substitution x , were investigated. Peculiarities of the Raman spectra, which are associated with magnetic ordering in $\text{HoFe}_{1.5}\text{Ga}_{1.5}(\text{BO}_3)_4$, $\text{HoFe}_2\text{Ga}(\text{BO}_3)_4$, and $\text{HoFe}_{2.5}\text{Ga}_{0.5}(\text{BO}_3)_4$ crystals, were detected.



I. INTRODUCTION

The ferrobates with the huntite structure with the general formula of $\text{LnFe}_3(\text{BO}_3)_4$ ($\text{Ln} = \text{rare-earth cation or Y}$) are the objects of many studies due to the wide range of promising physical properties. They are multiferroic, combining the mutual influence of magnetic and electrical subsystems.¹ Among other borates with the structure of the huntite (gallium borates,^{2–4} aluminum borates,^{5–7} scandium borates^{8,9}), iron borates are by far the most studied. A feature of these compounds is cascades of structural, magnetic, and spin-orientation phase transitions (the rare-earth ion type determines the presence of a particular type of phase transition).^{10–15}

The main objects of study of this work are new, previously unexplored, solid solutions of $\text{HoFe}_{3-x}\text{Ga}_x(\text{BO}_3)_4$. These compounds were chosen as objects of research to pay particular attention to the structural phase transition R32 \rightarrow P3₁21, realized in iron borates, and to its evolution due to the replacement of $\text{Fe}^{3+} \rightarrow \text{Ga}^{3+}$.

It is known that the structural phase transition R32 \rightarrow P3₁21 is observed in iron borates with huntite structure. As a result of this phase transition, the structure undergoes some changes: the $[\text{BO}_3]^{6-}$ group tilt angle changes, and two nonequivalent positions of iron cations arise, resulting in an increase in the unit cell volume by a factor of 3. The phase transition temperature essentially depends on the grade of the rare-earth ion—a linear dependence of the temperature T_c on the radius of the rare-earth

ion is observed—as the ionic radius increases, the phase transition temperature decreases. The structural phase transition is realized in ferrobates with rare-earth cations, the ionic radii of which lie in the range of 0.9–0.95 Å (namely, with $\text{Ln} = \text{Eu–Ho, Y}$).^{16–19}

This phase transition is not realized in other huntites, including gallium, regardless of the grade of the rare-earth cation. The main objective of this work is to study the features of the above phase transition in $\text{HoFe}_{3-x}\text{Ga}_x(\text{BO}_3)_4$ compounds with $x = 0.5, 1,$ and 1.5 using X-ray diffraction analysis and Raman spectroscopy based on a comparison of the data obtained for the indicated compositions, as well as with unsubstituted compounds $\text{HoGa}_3(\text{BO}_3)_4$ and $\text{HoFe}_3(\text{BO}_3)_4$.

II. FLUX GROWTH

In this paragraph, the questions related to control crystal nucleation of trigonal phases $\text{HoFe}_{3-x}\text{Ga}_x(\text{BO}_3)_4$ ($0 < x < 3$) in $\text{Bi}_2\text{Mo}_3\text{O}_{12} - \text{B}_2\text{O}_3 - \text{Ho}_2\text{O}_3 - \text{Fe}_2\text{O}_3 - \text{Ga}_2\text{O}_3$ flux system are considered. Special attention is given to metastability and phase dynamics of labile states on the border with accompanying

Received: October 17, 2019

Revised: January 5, 2020

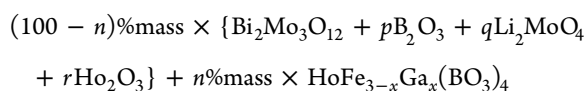
Published: January 9, 2020

Table 1. Main Crystallization Parameters for the Fluxes with $p = 3$ and $r = 0.6$

flux composition in the quasibinary form $(100 - n)\% \text{mass} \times \{\text{Bi}_2\text{Mo}_3\text{O}_{12} + p\text{B}_2\text{O}_3 + r\text{Ho}_2\text{O}_3\} + n\% \text{mass} \times \text{HoFe}_{3-x}\text{Ga}_x(\text{BO}_3)_4$									
crystal	n	p	r	x	$T_{\text{sat}}/^\circ\text{C}$	$dT_{\text{sat}}/dn, ^\circ\text{C}/\% \text{mass}$	$\Delta T_{\text{met}}/^\circ\text{C}$	accompanying phases	
$\text{HoFe}_3(\text{BO}_3)_4$	23	3	0.6	0	962	2.5	~12	$\alpha\text{-Fe}_2\text{O}_3, \text{Fe}_3\text{BO}_6$	
$\text{HoFe}_{2.5}\text{Ga}_{0.5}(\text{BO}_3)_4$	25	3	0.6	0.5	965	4.0			
$\text{HoFe}_2\text{Ga}(\text{BO}_3)_4$	25.5	3	0.6	1	985	4.8			
$\text{HoFe}_{1.5}\text{Ga}_{1.5}(\text{BO}_3)_4$	24	3	0.4	1.5	980	3.6			
$\text{HoGa}_3(\text{BO}_3)_4$	23	3	0.4	3	968	3.0			

phases. The technique of single crystals $\text{HoFe}_{3-x}\text{Ga}_x(\text{BO}_3)_4$ group growth on seeds is offered.

1. Phase Formation. The investigated flux system is more convenient to write in the quasi binary form



where n is a crystal-forming oxides concentration, corresponding to $\text{HoFe}_{3-x}\text{Ga}_x(\text{BO}_3)_4$ stoichiometry, and the p , q , and r parameters indicate the content of oxides over stoichiometry. Fluxes with various p , q , r , and n values and weight of 100 g are prepared at $T = 1000\text{--}1100\text{ }^\circ\text{C}$ by consecutive oxides melting [Bi_2O_3 (reagent grade), MoO_3 (analytical grade)], B_2O_3 (special purity grade), [Fe_2O_3 (special purity grade), Ho_2O_3 (domestic reagents)] + Ga_2O_3 (special-purity grade) and Li_2CO_3 (analytical grade) in platinum cylindrical crucible with a 50 mm diameter and 60 mm height. Then the crucible with the prepared flux was located into the furnace with the temperature field, which vertical component at $T = 1000\text{ }^\circ\text{C}$ decreases with a gradient $2\text{--}3\text{ }^\circ\text{C}/\text{cm}$ at removal from a bottom crucible. After flux homogenization at $T = 1000\text{ }^\circ\text{C}$ within 24 h, the temperature was lowered to the expected saturation temperature (T_{sat}), and a platinum crystal carrier in the form of a core with diameter of 4 mm was dipped into the flux. In 1–2 h the crystal carrier was withdrawn, and the nucleation on it was estimated. Further, these probes were continued with a $10\text{--}20\text{ }^\circ\text{C}$ temperature fall step, down to $T \approx 850\text{ }^\circ\text{C}$ without flux overheat.

It is established that hematite ($\alpha\text{-Fe}_2\text{O}_3$) is solo crystallizing phase at $p = q = r = 0$ and $n = 10\text{--}25$ in the range from its T_{sat} to $850\text{ }^\circ\text{C}$. With an increase of B_2O_3 and Ho_2O_3 content, accordingly to $p = 2$ and $r = 0.4$, hematite remains a high-temperature phase, and Fe_3BO_6 crystallite appears in the lower part of a temperature interval. Trigonal $\text{HoFe}_3(\text{BO}_3)_4$ becomes a high-temperature phase with a wide stability range only at $p = 2.5\text{--}3$ and $r = 0.5\text{--}0.6$. $\alpha\text{-Fe}_2\text{O}_3$ and Fe_3BO_6 phases keep the tendency to formation, but they appear near to the lower border of $\text{HoFe}_3(\text{BO}_3)_4$ metastability zone, and in some time after formation they start to be dissolved (“nonequilibrium effect”). Nonequilibrium effect and time of its relaxation were estimated, observing behavior of the equilibrium and labile phases simultaneously dipped in the flux. At temperature on $12\text{ }^\circ\text{C}$ below $\text{HoFe}_{3-x}\text{Ga}_x(\text{BO}_3)_4$ formation, the appreciable dissolution of $\alpha\text{-Fe}_2\text{O}_3$ and Fe_3BO_6 was observed in 10–15 h, and with overcooling increase to $20\text{ }^\circ\text{C}$ this time exceeded the day. The overcooling threshold value, since which any labile phase or both simultaneously were nucleated, essentially depended on parameters p , q , and r . That additionally narrowed a range of a possible choice of values for p , q , and r and demanded acceptance of measures to a nonadmission of their appreciable deviation during flux preparation, particularly, because of uncontrollable composition change at the evaporation.

The main crystallization parameters for the fluxes with $p = 3$ and $r = 0.6$ are shown in Table 1.

At crystal-forming oxides concentration of $n \approx 25\%$ the saturation temperature is smaller than $1000\text{ }^\circ\text{C}$, by that uncontrollable crystallization condition changes are excluded thereby during long-term working with the opened crucible. The specified width of a metastable zone $\Delta T_{\text{met}} \approx 12\text{ }^\circ\text{C}$ corresponds to 20 h of endurance of flux in the overcooled state without spontaneous crystals. With an increase of endurance time, it did not vary practically, and consequently it is possible to consider it long-term. At temperatures lower than $870\text{ }^\circ\text{C}$ the crystallization is ineffective because of increasing viscosity of the flux and permissible overcooling (narrowing ΔT_{met}).

2. Single-Crystal Growth. The Account Nonequilibrium Effect. The initial crystals growth process in spontaneous formation regime can be conventionally divided into two stages. On the first stage, at flux overcooling to $\Delta T > \Delta T_{\text{met}}$ the probability of formation and growth rate of labile phases are above that of $\text{HoFe}_{3-x}\text{Ga}_x(\text{BO}_3)_4$ ones. It causes the reduction of $\text{HoFe}_{3-x}\text{Ga}_x(\text{BO}_3)_4$ crystallite nucleation quantity; the crystal growth rate is slowed, and intergrowth with accompanying phase crystallite is possible. At the second stage, dissolution of labile phases begins, and $\text{HoFe}_{3-x}\text{Ga}_x(\text{BO}_3)_4$ growth rate increases also that faster, greater than the initial overcooling.

Since the quantity of growing crystals in the regime with spontaneous nucleation is not known, it is impossible to set the optimum subsequent temperature lowered rate. The crystal growth process in the regime with the use of seeds is most controllable. In this case, initial overcooling and subsequent temperature lowered rate should be set so that critical overcooling $\Delta T_{\text{init}} < \Delta T_{\text{crit}} = 10\text{--}15\text{ }^\circ\text{C}$ was not reached. On the one hand, infringement of this condition can result in competing phase formation, both on crystal carrier and at a crucible bottom and walls. In both cases crystallization control is lost. On the other hand, realization of a regime with labile phase preliminary spontaneous crystallization is not excluded. Thus, seeds growth rates will be more, while their growth is fed with a dissolved labile phase.

2.1. Seeds Production. At $T = 1000\text{ }^\circ\text{C}$ the crystal carrier was dipped into flux, and it was recessively rotated at 30 rpm. The furnace temperature was lowered to $T = T_{\text{sat}} - 12\text{ }^\circ\text{C}$. After 2 h in the crystal carrier, it was withdrawn from the furnace. Thus, on it crystallites were formed of a cooled flux enveloping crystal carrier. Then the crystal carrier was again dipped into the flux (without overheating at the same temperature $T = T_{\text{sat}} - 12\text{ }^\circ\text{C}$) and rotated at 30 rpm with every minute reverse. In the next 24 h 10–30 crystals with 0.5–2 mm size grew on it. They had high quality, and after withdrawal they were used as seed material.

2.2. Crystal Growth on Seeds. The crystal carrier with four qualitative seeds $\sim 1\text{ mm}$ in size was suspended above flux at $T = 1000\text{ }^\circ\text{C}$. After the temperature decreased to $T = T_{\text{sat}} + 7\text{ }^\circ\text{C}$ the crystal carrier with seeds was dipped into the flux to 15–20 mm

Table 2. Main Parameters of Processing and Refinement of the $\text{HoFe}_{(3-x)}\text{Ga}_x(\text{BO}_3)_4$ Samples

x	T , K	space group	cell parameters (Å), cell volume (\AA^3)	R_{wp}, R_p (%), χ^2	R_B (%)
0	143	$P3_121$	$a = 9.5256$ (2), $c = 7.5472$ (2), $V = 593.06$ (2)	2.48, 1.90, 1.32	2.16
	303	$P3_121$	$a = 9.5298$ (1), $c = 7.5557$ (1), $V = 594.25$ (2)	2.49, 1.82, 1.33	3.50
	403	$R32$	$a = 9.5397$ (1), $c = 7.5650$ (1), $V = 596.22$ (2)	2.55, 1.85, 1.34	3.70
	503	$R32$	$a = 9.5414$ (1), $c = 7.5736$ (1), $V = 597.11$ (2)	2.53, 1.86, 1.32	3.62
0.5	143	$P3_121$	$a = 9.5154$ (1), $c = 7.5319$ (1), $V = 590.59$ (2)	2.59, 1.91, 1.35	3.07
	303	$R32$	$a = 9.5261$ (1), $c = 7.5431$ (1), $V = 592.80$ (2)	2.67, 1.97, 1.38	3.30
	403	$R32$	$a = 9.5274$ (1), $c = 7.5505$ (1), $V = 593.55$ (2)	2.65, 1.94, 1.37	3.02
	503	$R32$	$a = 9.5293$ (2), $c = 7.5589$ (2), $V = 594.44$ (3)	3.40, 2.60, 1.22	3.14
1	143	$R32$	$a = 9.4915$ (2), $c = 7.4986$ (1), $V = 585.04$ (2)	2.93, 2.21, 1.39	1.01
	303	$R32$	$a = 9.4933$ (2), $c = 7.5039$ (1), $V = 585.67$ (2)	3.94, 3.03, 1.26	2.34
	403	$R32$	$a = 9.4946$ (2), $c = 7.5116$ (1), $V = 586.43$ (2)	3.95, 3.05, 1.25	1.99
	503	$R32$	$a = 9.4959$ (2), $c = 7.5197$ (1), $V = 587.22$ (2)	4.47, 3.26, 1.41	3.82
1.5	303	$R32$	$a = 9.4939$ (1), $c = 7.5081$ (1), $V = 586.06$ (2)	3.27, 2.43, 1.43	2.85
	403	$R32$	$a = 9.4954$ (1), $c = 7.5161$ (1), $V = 586.89$ (2)	3.16, 2.38, 1.37	2.31
	503	$R32$	$a = 9.4965$ (2), $c = 7.5239$ (1), $V = 587.62$ (2)	3.22, 2.41, 1.38	2.81
3	303	$R32$	$a = 9.44330$ (8), $c = 7.43662$ (7), $V = 574.32$ (1)	6.22, 4.55, 2.12	3.84
	403	$R32$	$a = 9.44453$ (8), $c = 7.4483$ (8), $V = 575.10$ (1)	6.00, 4.42, 2.04	3.72
	503	$R32$	$a = 9.44608$ (9), $c = 7.45292$ (8), $V = 575.92$ (1)	3.22, 2.41, 1.38	2.81

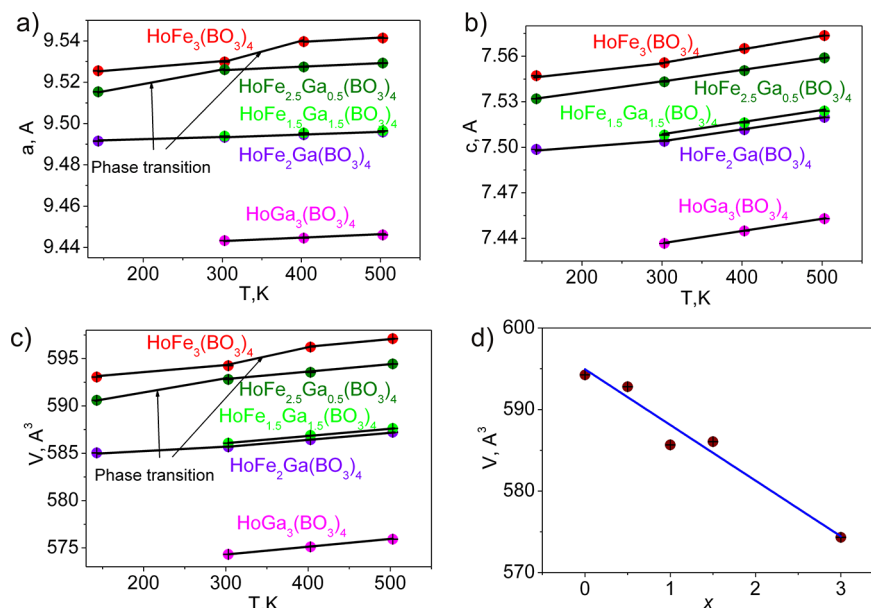


Figure 1. Cell parameters dependences per T for all compounds: (a) $a(T)$; (b) $c(T)$; (c) $V(T)$. Cell volume V of $\text{HoFe}_{(3-x)}\text{Ga}_x(\text{BO}_3)_4$ compounds per concentration x .

depth, and reverse rotation with a speed of 30 rpm and a 1 min period was switched on. After 15 min, the temperature decreased to $T = T_{\text{sat}} - 5$ °C. Furthermore, the temperature gradually decreased at 1 °C/d rate. In 9–13 d, the growth process was finished. Crystal carrier was lifted above flux and cooled to room temperature with the furnace supply switched off. As a result, crystals approximately the 6–10 mm sizes sufficient for physical research are grown. Spontaneous formation and other phases were absent.

III. POWDER X-RAY DIFFRACTION

The powder diffraction data of $\text{HoFe}_{(3-x)}\text{Ga}_x(\text{BO}_3)_4$ ($x = 0, 0.5, 1, 1.5, 3$) for Rietveld analysis were collected at 303, 403, and 503 K with a Bruker D8 Advance powder diffractometer (Cu $K\alpha$ radiation) and linear VANTEC detector. The samples $x = 0$, $x = 0.5$, and $x = 1$ were additionally measured at 143 K. The step size of 2θ was 0.016°, and the counting time was 0.5 s per step.

Rietveld refinement was performed by using TOPAS 4.2.²⁰ All peaks of all phases were indexed by trigonal cell ($R32$) with parameters close to $\text{GdFe}_3(\text{BO}_3)_4$.²¹ Superstructure peaks of low-temperature phases ($x = 0.5$, $T = 143$ K, $P3_121$ and $x = 0$, $T = 303$ K, $P3_121$) were not detected due to small exposition time. Anyway, $R32$ and $P3_121$ phases were used as a starting model for Rietveld refinement at high- and low-temperature phases. The site of the Gd ion was occupied by Ho ion, and the site of Fe was replaced by Fe/Ga ions with fixed occupations according to suggested chemical formula.

Refinement was stable and gave low R -factors (Table 2). Linear decreasing of cell volume per concentration $V(x)$ (Figure 1d) is in a good agreement with smaller ion radii (I_R) of Ga^{3+} ion $I_R(\text{Ga}^{3+}, \text{CN} = 6) = 0.62$ Å in comparison with $I_R(\text{Fe}^{3+}, \text{CN} = 6) = 0.645$ Å (CN = coordination number). Therefore, it proves that the suggested chemical composition is close to the real one. Cell parameters of all compounds were plotted per T (Figure

Table 3. Expansion Coefficients α_a , α_c , and α_v for All Compounds in Different Temperature Ranges

x	α_a (10^{-6} K^{-1})			α_c (10^{-6} K^{-1})			α_v (10^{-6} K^{-1})		
	143–303K	303–403K	403–503K	143–303K	403–503K	303–503 K	143–303 K	403–503K	303–503 K
0	2.8	10.4	1.8	5.6	12.3	11.4	12.5	33.2	14.9
0.5	7.0	1.7		9.3	10.5		23.4	13.8	
1	1.2	1.4		4.4	10.5		6.7	13.2	
1.5		1.4			10.5			13.3	
3		1.5			11.0			13.9	

Table 4. Wyckoff Positions and Irreducible Representations (Γ -Point Phonon Modes) of $\text{HoFe}_3(\text{BO}_3)_4$ and $\text{HoGa}_3(\text{BO}_3)_4$ Crystals^a

Atom		Wyckoff	Γ -point phonon modes
Space group: $R32$ (No. 155)		position	
Point group: $D3$			
Ho		3a	$A_2 + E$
Fe (Ga)		9d	$A_1 + 2 A_2 + 3 E$
O		9e	$A_1 + 2 A_2 + 3 E$
O		9e	$A_1 + 2 A_2 + 3 E$
O		18f	$3 A_1 + 3 A_2 + 6 E$
B		3b	$A_2 + E$
B		9e	$A_1 + 2 A_2 + 3 E$
Modes classifications			
$\Gamma_{\text{Raman}} = 7 A_1 + 19 E$	$\Gamma_{\text{IR}} = 12 A_2 + 19 E$	$\Gamma_{\text{ac}} = A_2 + E$	$\Gamma_{\text{Mechanical}} = 7 A_1 + 13 A_2 + 20 E$
Raman tensor			
$A_1 = \begin{bmatrix} a & 0 & 0 \\ 0 & a & 0 \\ 0 & 0 & b \end{bmatrix} \quad E(x) = \begin{bmatrix} c & 0 & 0 \\ 0 & -c & d \\ 0 & d & 0 \end{bmatrix} \quad E(y) = \begin{bmatrix} 0 & -c & -d \\ -c & 0 & 0 \\ -d & 0 & 0 \end{bmatrix}$			

^aSpace group: $R32$, No. 155.

1a–c). One can see the break of $a(T)$ and $V(T)$ parameters for $x = 0$ and $x = 0.5$, which can be associated with well-known phase transition $R32 \leftrightarrow P3_121$.¹² Note that all cell parameters are increased under heating and that the expansion coefficients α_a , α_c , and α_v in the range of 303–503 K are close to each other for all compounds (Table 3). Only phase transitions change α values.

IV. RAMAN SPECTROSCOPY STUDY AND AB INITIO CALCULATION

Single crystals of $\text{HoFe}_{3-x}\text{Ga}_x(\text{BO}_3)_4$ ($x = 0, 0.75$) were used to obtain Raman spectra that were recorded with a Horiba Jobin Yvon T64000 triple spectrometer equipped with a liquid nitrogen-cooled charge-coupled device (CCD) detection system in subtractive dispersion mode using backscattering geometry. Ar+ ion laser Spectra-Physics Stabilite 2017 with $\lambda =$

Table 5. Wyckoff Positions and Irreducible Representations (Γ -Point Phonon Modes) of $\text{HoFe}_3(\text{BO}_3)_4$ ^a

Atom	Wyckoff position	Γ -point phonon modes
Space group: P3 ₁ 21 (No. 152)		
Point group: D ₃		
Ho	3a	$A_1 + 2 A_2 + 3 E$
Fe	6c	$3 A_1 + 3 A_2 + 6 E$
Fe	3a	$A_1 + 2 A_2 + 3 E$
O	6c	$3 A_1 + 3 A_2 + 6 E$
O	6c	$3 A_1 + 3 A_2 + 6 E$
O	6c	$3 A_1 + 3 A_2 + 6 E$
O	6c	$3 A_1 + 3 A_2 + 6 E$
O	6c	$3 A_1 + 3 A_2 + 6 E$
O	3b	$A_1 + 2 A_2 + 3 E$
O	3b	$A_1 + 2 A_2 + 3 E$
B	3b	$A_1 + 2 A_2 + 3 E$
B	6c	$3 A_1 + 3 A_2 + 6 E$
B	3b	$A_1 + 2 A_2 + 3 E$
Modes classifications		
$\Gamma_{\text{Raman}} = 27 A_1 + 59 E$	$\Gamma_{\text{IR}} = 32 A_2 + 59 E$	$\Gamma_{\text{ac}} = A_2 + E$
$\Gamma_{\text{Mechanical}} = 27 A_1 + 33 A_2 + 60 E$		
Raman tensor		
$A_1 = \begin{bmatrix} a & 0 & 0 \\ 0 & a & 0 \\ 0 & 0 & b \end{bmatrix} \quad E(x) = \begin{bmatrix} c & 0 & 0 \\ 0 & -c & d \\ 0 & d & 0 \end{bmatrix} \quad E(y) = \begin{bmatrix} 0 & -c & -d \\ -c & 0 & 0 \\ -d & 0 & 0 \end{bmatrix}$		

^aSpace group: P3₁21, No. 152.

514.5 nm and 5 mW power on a sample was used as an excitation light source.

Temperature measurements were performed with a closed-cycle ARS CS204-X1.SS helium cryostat in the temperature range of 8–400 K. The temperature was monitored by

LakeShore DT-6SD1.4L silicon diode. During experiments, the cryostat was evacuated to 1×10^{-6} mbar. Spectroscopic measurements were performed in the subtractive dispersion mode, which attained a low-wavenumber limit of 8 cm^{-1} in the present setup, for investigation of the low-wavenumber spectra.

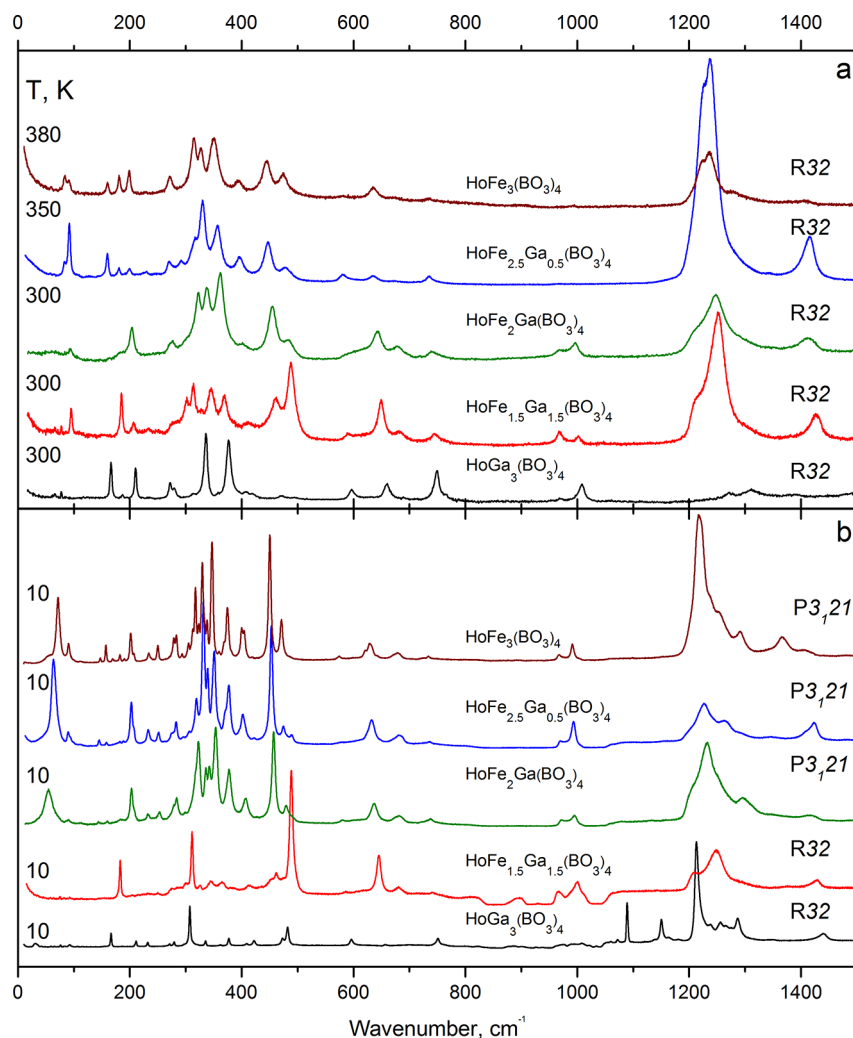


Figure 2. Raman spectra of $\text{HoFe}_{3-x}\text{Ga}_x(\text{BO}_3)_4$ crystals: (a) R32 phase, (b) low-temperature phase.

The deformation of the low-wavenumber spectral edge by an optical slit, which sometimes smears the true features of low-wavenumber spectra, was carefully eliminated by rigorous optical alignment. CCD pixel coverage in subtractive dispersion mode was as fine as 0.3 cm^{-1} , but it was limited by spectrometer's spectral resolution of 2 cm^{-1} .

The temperature experiments were performed in the dynamic regime by varying the sample temperature. The rate of temperature variation was 0.7 K/min . The uncertainty of the measured temperature for a given rate can be estimated as the difference between adjacent measurements, and it was $\pm 0.13 \text{ K}$ in one spectrum measurement. The overall time for a single spectrum accumulation was within 30 s . The spectra were acquired with a temperature step of 0.4 K . This measurement protocol was the same as that described in ref 22. The spectra were deconvolved into separate spectral lines, to obtain quantitative information. To describe the line shapes, we used the Lorentz function. Experimental Raman spectra were processed quantitatively using conventional damped harmonic oscillator (DHO) functions:²³

$$I(\omega) = F(\omega, T) \cdot \sum_i \frac{2A_i \omega_{0i}^2 \gamma_i \omega}{(\omega_{0i}^2 - \omega^2)^2 + 4\gamma_i^2 \omega^2}$$

where ω is current wavenumber, A , ω_0 , and γ denote the intensity, harmonic wavenumber of the band center, and full width at half-maximum, respectively. The temperature factor $F(\omega, T)$ is calculated by

$$F(\omega, T) = \begin{cases} n(\omega) + 1 & \text{Stokes} \\ n(\omega) & \text{anti-Stokes} \end{cases}$$

$$n(\omega) = \left[\exp\left(\frac{\hbar\omega}{k_B T}\right) - 1 \right]^{-1}$$

with the intensity interplay between the Stokes and anti-Stokes parts near 0 cm^{-1} uniquely obtained according to the temperature; \hbar , k_B are the reduced Planck constant and the Boltzmann constant, respectively. The present Raman setup observes only the Stokes component. We used seven DHO functions for spectral fitting in the range of $10\text{--}300 \text{ cm}^{-1}$.

The factor-group analysis was performed to find the symmetries of modes using the local symmetry of all the atomic positions. The high-temperature structure of $\text{HoFe}_3(\text{BO}_3)_4$ and $\text{HoGa}_3(\text{BO}_3)_4$ contains 20 atoms in a primitive cell and, as a result of that, 60 normal modes. Three of them are acoustical with A_2 and E symmetry. The 57 optical modes are there. The 26 Raman modes include 7 modes of A_1 symmetry and 19 doubly

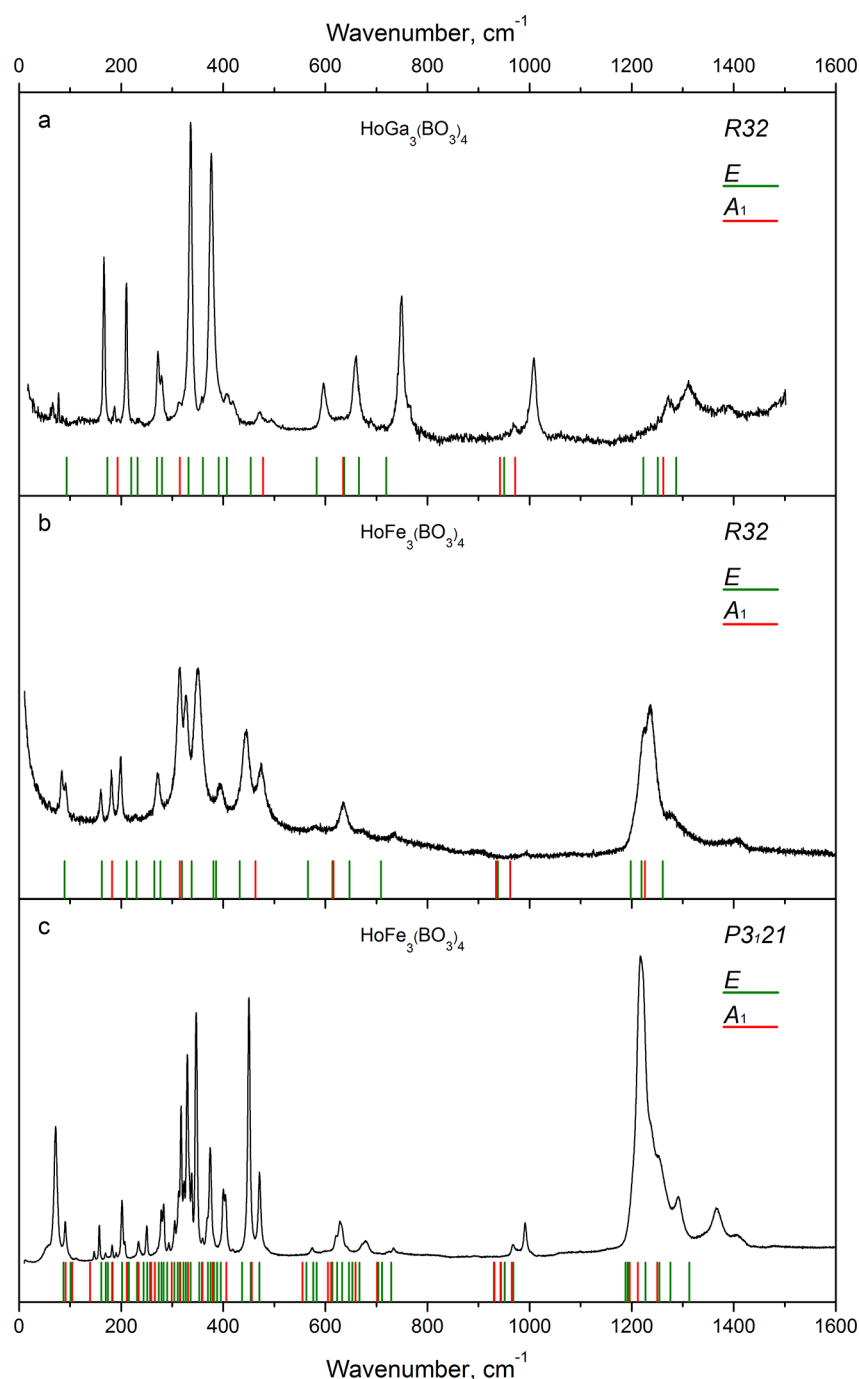


Figure 3. Experimental Raman spectra of the crystals: (a) $\text{HoGa}_3(\text{BO}_3)_4$ in R32 phase, (b) $\text{HoFe}_3(\text{BO}_3)_4$ in R32 phase, (c) $\text{HoFe}_3(\text{BO}_3)_4$ in P3₁21 phase; calculated wavenumbers presented by colored bars: green – E symmetry, red – A₁ symmetry.

degenerated E modes. The vibrational modes symmetry analysis of the R32 structure of $\text{HoFe}_3(\text{BO}_3)_4$ and $\text{HoGa}_3(\text{BO}_3)_4$ crystals is presented in Table 4. According to the group-theoretical analysis, holmium atoms in position 3a and boron atoms in position 3b included only in doubly degenerated Raman active E modes in phase R32 in $\text{HoFe}_3(\text{BO}_3)_4$ and $\text{HoGa}_3(\text{BO}_3)_4$ crystals.

The primitive cell of the low-temperature structure of $\text{HoFe}_3(\text{BO}_3)_4$ crystal contains three formula units. The low-temperature structure of $\text{HoFe}_3(\text{BO}_3)_4$ contains 60 atoms in a primitive cell and, as a result of that, 180 normal modes. Three of them are acoustical with A₂ and E symmetry. The 177 optical modes are there. The 86 Raman modes include 27 modes of A₁

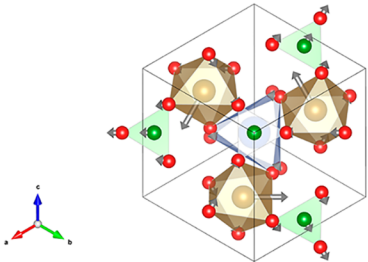
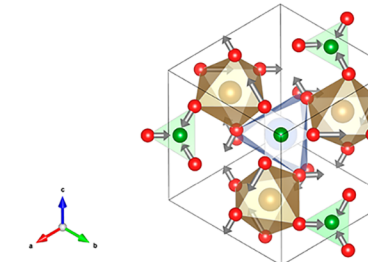
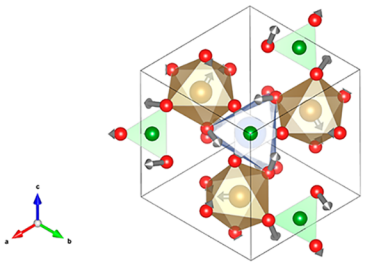
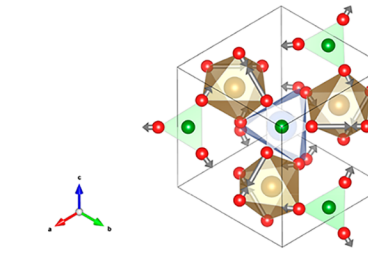
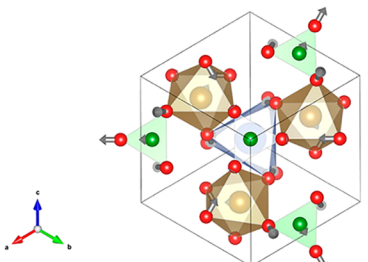
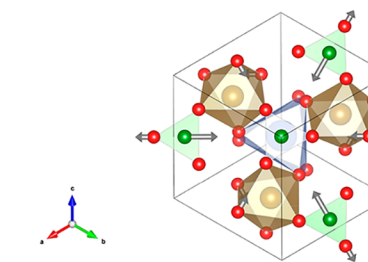
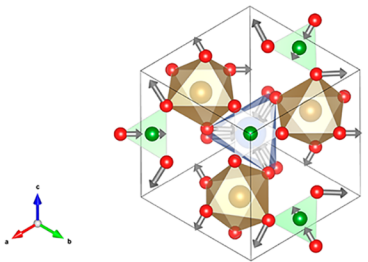
symmetry and 59 doubly degenerated E modes. The fully symmetric A₁ modes are active in the Raman spectra and not active in the IR spectra.

The vibrational modes symmetry analysis of the P3₁21 structure of $\text{HoFe}_3(\text{BO}_3)_4$ crystal is presented in Table 5.

The B–O bond strengths inside BO_3 triangular ions exceed the bond strengths of these ions with the cation sublattice. There are two types of $(\text{BO}_3)^{3-}$ ions: with the D₃ and C₂ positional symmetry in the high-temperature phase of $\text{HoFe}_3(\text{BO}_3)_4$ and $\text{HoGa}_3(\text{BO}_3)_4$ crystals.

The Raman spectra of $\text{HoFe}_{3-x}\text{Ga}_x(\text{BO}_3)_4$ crystals in high-temperature R32 phase and low-temperature phases are presented in Figure 2. In the $\text{HoFe}_{3-x}\text{Ga}_x(\text{BO}_3)_4$ solid solutions,

Table 6. Calculated Wavenumbers of the A_1 Modes in the $\text{HoFe}_3(\text{BO}_3)_4$ Crystal, Forms of the Vibrations

<p>182 cm^{-1}</p>  <p>Diagram showing the crystal structure of $\text{HoFe}_3(\text{BO}_3)_4$ with displacement arrows for the 182 cm^{-1} vibrational mode. A small 3D coordinate system (x, y, z) is shown in the bottom left corner.</p>	<p>934 cm^{-1}</p>  <p>Diagram showing the crystal structure of $\text{HoFe}_3(\text{BO}_3)_4$ with displacement arrows for the 934 cm^{-1} vibrational mode. A small 3D coordinate system (x, y, z) is shown in the bottom left corner.</p>
<p>315 cm^{-1}</p>  <p>Diagram showing the crystal structure of $\text{HoFe}_3(\text{BO}_3)_4$ with displacement arrows for the 315 cm^{-1} vibrational mode. A small 3D coordinate system (x, y, z) is shown in the bottom left corner.</p>	<p>962 cm^{-1}</p>  <p>Diagram showing the crystal structure of $\text{HoFe}_3(\text{BO}_3)_4$ with displacement arrows for the 962 cm^{-1} vibrational mode. A small 3D coordinate system (x, y, z) is shown in the bottom left corner.</p>
<p>463 cm^{-1}</p>  <p>Diagram showing the crystal structure of $\text{HoFe}_3(\text{BO}_3)_4$ with displacement arrows for the 463 cm^{-1} vibrational mode. A small 3D coordinate system (x, y, z) is shown in the bottom left corner.</p>	<p>1226 cm^{-1}</p>  <p>Diagram showing the crystal structure of $\text{HoFe}_3(\text{BO}_3)_4$ with displacement arrows for the 1226 cm^{-1} vibrational mode. A small 3D coordinate system (x, y, z) is shown in the bottom left corner.</p>
<p>616 cm^{-1}</p>  <p>Diagram showing the crystal structure of $\text{HoFe}_3(\text{BO}_3)_4$ with displacement arrows for the 616 cm^{-1} vibrational mode. A small 3D coordinate system (x, y, z) is shown in the bottom left corner.</p>	<p>Red circles – Oxygen</p> <p>Green circles – Boron</p> <p>Big brown circles – Iron (Ferrum)</p> <p>Big grey circles – Holmium</p>

the substitution of the Fe ion for Ga slightly affects the spectra of the high-temperature phase R32. As the temperature decreases, some crystals undergo the structural phase transition; this is seen in the spectra at a temperature of 10 K (Figure 2b). After the phase transition, the number of lines in the Raman spectrum increases significantly in the $\text{HoFe}_2\text{Ga}(\text{BO}_3)_4$, $\text{HoFe}_{2.5}\text{Ga}_{0.5}(\text{BO}_3)_4$, and $\text{HoFe}_3(\text{BO}_3)_4$ crystals. However, the number of lines in the spectra of the $\text{HoFe}_{1.5}\text{Ga}_{1.5}(\text{BO}_3)_4$ and $\text{HoGa}_3(\text{BO}_3)_4$ crystals is practically unchanged at 10 K.

First-principle calculations were performed using the projector-augmented wave (PAW) method²⁴ within density functional theory (DFT), as implemented in the VASP code.²⁵ We used the generalized gradient approximation (GGA) functional with Perdew–Burke–Ernzerhof (PBE) parametrization.²⁶ Electronic configurations were chosen as follows: Ho, $5d^6 6s^1 6p^2$; Ga, $4s^2 4p^1$; Fe, $3d^7 4s^1$; B, $2s^2 2p^1$; and O, $2s^2 2p^4$. The plane-wave cutoff was set at 600 eV. The size of the k-point mesh for Brillouin zone, based on the Monkhorst–Pack scheme,²⁷ was $7 \times 7 \times 7$. The GGA+U calculations within Dudarev's approach²⁸ were performed by applying a Hubbard-like potential for Fe d states. Ho 4f electrons were assumed as frozen in the core. Spin-polarized calculations were performed due to the presence of iron ions. Calculated wavenumbers for $\text{HoFe}_3(\text{BO}_3)_4$ and $\text{HoGa}_3(\text{BO}_3)_4$ crystals symmetry group R32 is presented in Supporting Information in the Tables S1 and S2, respectively. Calculated wavenumbers for $\text{HoFe}_3(\text{BO}_3)_4$ crystal symmetry group $P3_121$ are presented in Table S3.

The experimental and calculated spectra of crystals are presented in Figure 3. The calculated A_1 modes are shown in red, and doubly degenerate E modes are shown in green. The calculated wavenumbers are in satisfactory agreement with the wavenumbers obtained in the experiment. The forms of the A_1 modes of the $\text{HoFe}_3(\text{BO}_3)_4$ crystal in phase is shown in Table 6.

The experimental Raman band from 1200 to 1400 cm^{-1} corresponds to the excitation of four modes according to the calculation (Figure 3). Oxygen and boron atoms take part in these vibrations (Table 6). The calculated fully symmetric modes 934 and 962 cm^{-1} correspond to the vibrations of the crystal in the region of 1000 cm^{-1} (Figure 3). These modes include the displacements of the vertices of the planar BO_3 triangles and the movements of oxygen ions in the FeO_6 octahedra. Raman modes in the range from 550 to 800 cm^{-1} (Figure 3) include vibrations of oxygen and boron atoms in the BO_3 triangles, oxygen atoms in FeO_6 octahedra, and HoO_6 prisms (Table 6). Low-wavenumber Raman modes include lattice vibrations and displacement of heavy atoms in the crystal. In particular, the A_1 modes are vibrations of BO_3 triangles as a whole and the displacements of iron atoms (Table 6).

The structural soft modes condensation in $\text{HoFe}_2\text{Ga}(\text{BO}_3)_4$ and $\text{HoFe}_{2.5}\text{Ga}_{0.5}(\text{BO}_3)_4$ was observed. The maps of Raman intensity in the low-wavenumber part of the spectra are shown in Figure 4. We observe three modes in the low-frequency region in the $\text{HoFe}_2\text{Ga}(\text{BO}_3)_4$ crystal (Figure 4a). Modes 85 and 94 cm^{-1} shift slightly. The intensity of the 94 cm^{-1} mode increases with heating. The position of the soft mode moves on $\sim 50\text{ cm}^{-1}$ with heat. The position of the soft mode shifts by 65 cm^{-1} with heating in the $\text{HoFe}_{2.5}\text{Ga}_{0.5}(\text{BO}_3)_4$ crystal (Figure 4b). The mode position of 92 cm^{-1} changes to 95 cm^{-1} with cooling, and its intensity decreases. A new line in the spectrum arises after a structural phase transition. The intensity of the 91 cm^{-1} mode increases with cooling.

The magnetic phase transitions were previously detected in other crystals with a huntite structure containing iron atoms at

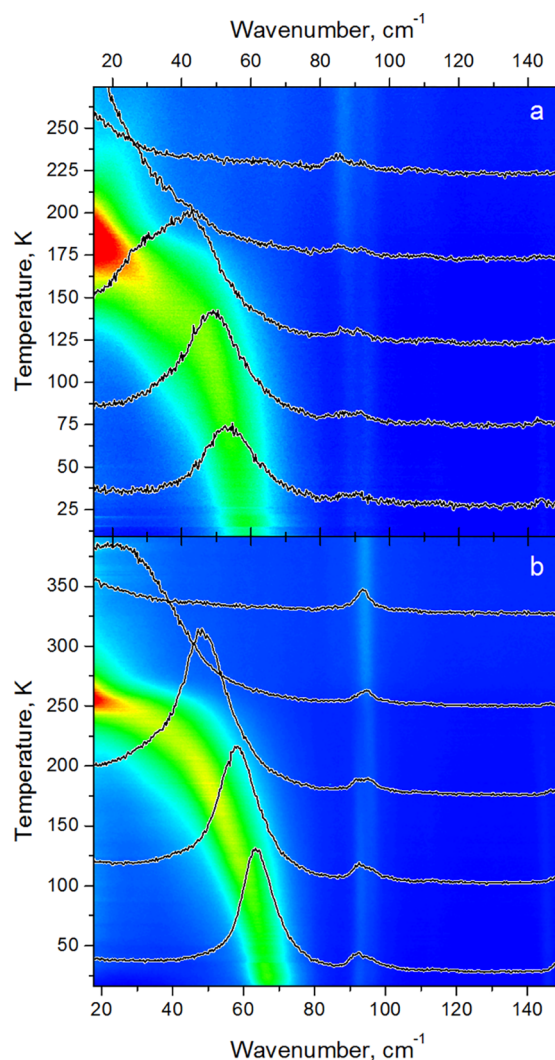


Figure 4. Maps of Raman intensity in the low-wavenumber part of spectra: (a) $\text{HoFe}_2\text{Ga}(\text{BO}_3)_4$ crystal, (b) $\text{HoFe}_{2.5}\text{Ga}_{0.5}(\text{BO}_3)_4$ crystal.

temperatures below 50 K .^{10,12,15–19} Therefore, in new crystals, we expected to see anomalies in the Raman spectra associated with magnetic ordering. We found a soft mode associated with magnetic ordering in the spectra of the $\text{HoFe}_{2.5}\text{Ga}_{0.5}(\text{BO}_3)_4$ crystal in the parallel polarization (Figure 5). The soft mode connected with magnetic ordering is visible at temperatures $\sim 30\text{ K}$. We did not find soft modes associated with magnetic ordering in $\text{HoFe}_2\text{Ga}(\text{BO}_3)_4$ and $\text{HoFe}_{1.5}\text{Ga}_{1.5}(\text{BO}_3)_4$ crystals. However, other anomalies associated with magnetic ordering were found in the high-frequency spectral regions (Figure 6). These regions of spectra include the vibrations of the vertices of the planar BO_3 triangles and the movements of oxygen ions in the FeO_6 octahedra. New modes of 973 cm^{-1} in the spectra of $\text{HoFe}_2\text{Ga}(\text{BO}_3)_4$ crystal (Figure 6a) and 960 cm^{-1} in the spectra of $\text{HoFe}_{1.5}\text{Ga}_{1.5}(\text{BO}_3)_4$ crystal (Figure 6b) appear at low temperatures. The spectra transformations of $\text{HoFe}_2\text{Ga}(\text{BO}_3)_4$ crystal with temperature decrease are presented in Figures S1–S4. The dependence of positions of two lines on the temperature in the Raman spectra of $\text{HoFe}_2\text{Ga}(\text{BO}_3)_4$ crystal is presented in Figure S5. The relation of intensities of 996 and 972 lines in the Raman spectra of $\text{HoFe}_2\text{Ga}(\text{BO}_3)_4$ crystal (Figure S6) changes noticeably at 28 K .

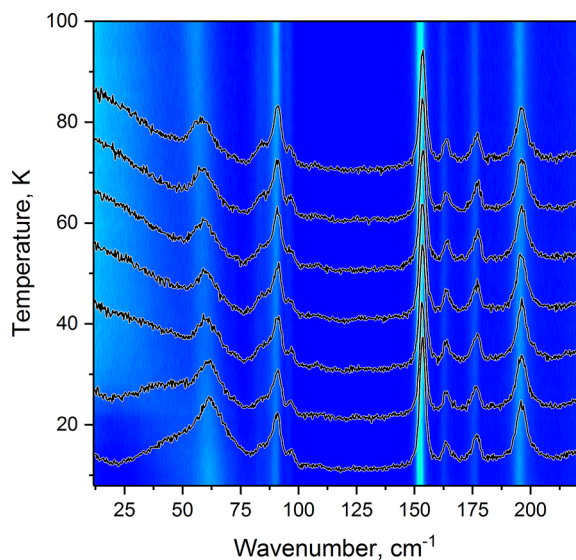


Figure 5. Raman intensity map in the low-wavenumber part of spectra: $\text{HoFe}_{2.5}\text{Ga}_{0.5}(\text{BO}_3)_4$ crystal.

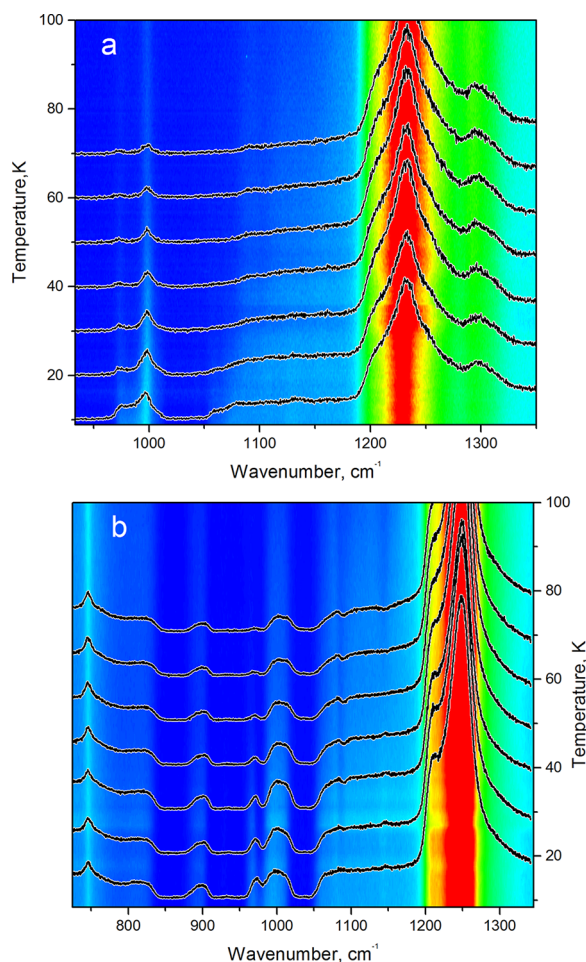


Figure 6. Maps of Raman intensity in the high-wavenumber part of spectra: (a) $\text{HoFe}_2\text{Ga}(\text{BO}_3)_4$ crystal, (b) $\text{HoFe}_{1.5}\text{Ga}_{1.5}(\text{BO}_3)_4$ crystal.

Figure 7 is the result of our studies of changes in the properties of $\text{HoFe}_{3-x}\text{Ga}_x(\text{BO}_3)_4$ solid solutions depending on the concentration of gallium ions. We determined the temperatures of structural phase transition in $\text{HoFe}_2\text{Ga}(\text{BO}_3)_4$ and

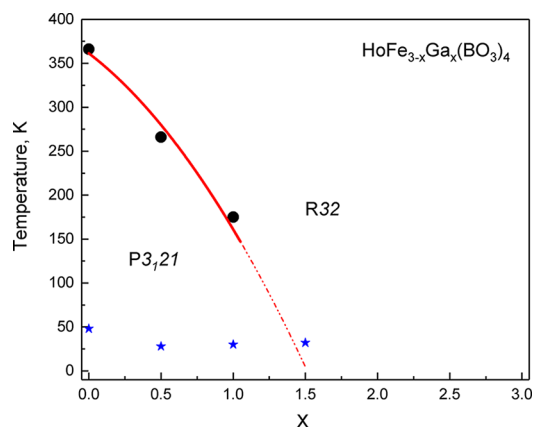


Figure 7. Phase diagram of Composition–Temperature of the $\text{HoFe}_{3-x}\text{Ga}_x(\text{BO}_3)_4$ crystals. (●) The points of structural phase transitions. (★) The points of magnetic phase transitions.

$\text{HoFe}_{2.5}\text{Ga}_{0.5}(\text{BO}_3)_4$ crystals. These points of structural phase transitions are shown in black circles (Figure 6). The temperatures of magnetic ordering of $\text{HoFe}_2\text{Ga}(\text{BO}_3)_4$, $\text{HoFe}_{2.5}\text{Ga}_{0.5}(\text{BO}_3)_4$, and $\text{HoFe}_{1.5}\text{Ga}_{1.5}(\text{BO}_3)_4$ are estimated from the manifestations of the interaction of structural and magnetic ordering in the Raman spectra. These points are shown by blue stars. The temperature of the structural and magnetic phase transitions in the $\text{HoFe}_3(\text{BO}_3)_4$ crystal is taken from the other articles.^{29,30} The temperature of the $\text{R32} \rightarrow \text{P3,21}$ structural phase transition decreases with increasing gallium concentration. The $\text{HoFe}_{1.5}\text{Ga}_{1.5}(\text{BO}_3)_4$ crystal remains in phase R32 when cooled to 10 K.

V. CONCLUSION

Single crystals of solid solutions of $\text{HoFe}_{3-x}\text{Ga}_x(\text{BO}_3)_4$ with $x = 0, 0.5, 1, 1.5,$ and 3 were obtained using flux synthesis. The three new $\text{HoFe}_{1.5}\text{Ga}_{1.5}(\text{BO}_3)_4$, $\text{HoFe}_2\text{Ga}(\text{BO}_3)_4$, and $\text{HoFe}_{2.5}\text{Ga}_{0.5}(\text{BO}_3)_4$ crystals were grown taking into account nonequilibrium effect. The structural properties of each of the synthesized samples were studied using X-ray powder diffraction analysis at the temperatures of 303, 403, and 503 K. The samples $x = 0, x = 0.5,$ and $x = 1$ were additionally measured at 143 K. The cell volume of solid solutions decreases with increasing gallium ions concentration. The Raman spectra of solid solutions $\text{HoFe}_{3-x}\text{Ga}_x(\text{BO}_3)_4$ were studied in the temperature range from 10 to 400 K. The vibrational spectra and eigenvectors of the $\text{HoFe}_3(\text{BO}_3)_4$ and $\text{HoGa}_3(\text{BO}_3)_4$ in the R32 phase and $\text{HoFe}_3\text{Ga}(\text{BO}_3)_4$ in the P3,21 phase were calculated within density functional theory. The calculated spectra are in a good agreement with the experimental data. The features of the Raman spectra of the $\text{HoFe}_2\text{Ga}(\text{BO}_3)_4$, $\text{HoFe}_{2.5}\text{Ga}_{0.5}(\text{BO}_3)_4$, and $\text{HoFe}_3(\text{BO}_3)_4$ crystals associated with the $\text{R32} \rightarrow \text{P3,21}$ structural phase transition, which have a strong dependence on the degree of substitution x , have been investigated. The temperature of the structural phase transition is ~ 177 K for $\text{HoFe}_2\text{Ga}(\text{BO}_3)_4$ and 266 K for $\text{HoFe}_{2.5}\text{Ga}_{0.5}(\text{BO}_3)_4$.

Magnetic ordering affects the behavior of the structural modes in crystals $\text{HoFe}_{1.5}\text{Ga}_{1.5}(\text{BO}_3)_4$, $\text{HoFe}_2\text{Ga}(\text{BO}_3)_4$, and $\text{HoFe}_{2.5}\text{Ga}_{0.5}(\text{BO}_3)_4$ in the low-temperature region. Peculiarities of the vibrational spectra, which are associated with magnetic ordering in $\text{HoFe}_{1.5}\text{Ga}_{1.5}(\text{BO}_3)_4$, $\text{HoFe}_2\text{Ga}(\text{BO}_3)_4$, and $\text{HoFe}_{2.5}\text{Ga}_{0.5}(\text{BO}_3)_4$ crystals, were detected. The temperature of the magnetic ordering was estimated: $T_n = 32$ K in

$\text{HoFe}_{1.5}\text{Ga}_{1.5}(\text{BO}_3)_4$, $T_n = 30$ K in $\text{HoFe}_2\text{Ga}(\text{BO}_3)_4$, and $T_n = 28$ K in $\text{HoFe}_{2.5}\text{Ga}_{0.5}(\text{BO}_3)_4$.

■ ASSOCIATED CONTENT

SI Supporting Information

The Supporting Information is available free of charge at <https://pubs.acs.org/doi/10.1021/acs.cgd.9b01387>.

Calculated vibrational frequencies, Raman spectra, Raman shifts plotted versus temperature (PDF)

■ AUTHOR INFORMATION

Corresponding Author

Svetlana Krylova – Kirensky Institute of Physics, FRC KSC SB RAS, Krasnoyarsk 660036, Russia; orcid.org/0000-0003-1277-6044; Email: slanky@iph.krasn.ru

Other Authors

Evgeniya Moshkina – Kirensky Institute of Physics, FRC KSC SB RAS, Krasnoyarsk 660036, Russia; Siberian State Aerospace University, Krasnoyarsk 660014, Russia; orcid.org/0000-0001-7250-0387

Irina Gudim – Kirensky Institute of Physics, FRC KSC SB RAS, Krasnoyarsk 660036, Russia

Maxim Molochev – Kirensky Institute of Physics, FRC KSC SB RAS, Krasnoyarsk 660036, Russia; Siberian Federal University, Krasnoyarsk 660041, Russia; Far Eastern State Transport University, Khabarovsk 680021, Russia

Vladislav Temerov – Kirensky Institute of Physics, FRC KSC SB RAS, Krasnoyarsk 660036, Russia

M. S. Pavlovskiy – Kirensky Institute of Physics, FRC KSC SB RAS, Krasnoyarsk 660036, Russia; Siberian Federal University, Krasnoyarsk 660041, Russia

Alexander Vtyurin – Kirensky Institute of Physics, FRC KSC SB RAS, Krasnoyarsk 660036, Russia; Siberian Federal University, Krasnoyarsk 660041, Russia

Alexander Krylov – Kirensky Institute of Physics, FRC KSC SB RAS, Krasnoyarsk 660036, Russia; orcid.org/0000-0001-8949-0584

Complete contact information is available at: <https://pubs.acs.org/doi/10.1021/acs.cgd.9b01387>

Notes

The authors declare no competing financial interest.

■ ACKNOWLEDGMENTS

The reported study was funded by the Russian Foundation for Basic Research No. 18-02-00754. The experiments were performed using equipment of Center for Common Use, Krasnoyarsk Scientific Center, FSC SB RAS.

■ REFERENCES

- (1) Vopson, M. M. Fundamentals of Multiferroic Materials and Their Possible Applications. *Crit. Rev. Solid State Mater. Sci.* **2015**, *40*, 223–250.
- (2) Al'shinskaya, L. I.; Leonyuk, N. I.; Timchenko, T. I. High-temperature crystallization, composition, structure, and certain properties of rare-earth gallium borates. *Krist. Tech.* **1979**, *14*, 897–903.
- (3) Borovikova, E. Yu.; Boldyrev, K. N.; Aksenov, S. M.; Dobretsova, E. A.; Kurazhkovskaya, V. S.; Leonyuk, N. I.; Savon, A. E.; Deyneko, D. V.; Ksenofontov, D. A. Crystal growth, structure, infrared spectroscopy, and luminescent properties of rare-earth gallium borates $\text{RGa}_3(\text{BO}_3)_4$ (R = Nd, Sm–Er, Y). *Opt. Mater.* **2015**, *49*, 304–311.

- (4) Volkov, N. V.; Gudim, I. A.; Eremin, E. V.; Begunov, A. I.; Demidov, A. A.; Boldyrev, K. N. Magnetization, magnetoelectric polarization, and specific heat of $\text{HoGa}_3(\text{BO}_3)_4$. *JETP Lett.* **2014**, *99*, 67.

- (5) Liang, K.-C.; Chaudhury, R. P.; Lorenz, B.; Sun, Y. Y.; Bezmaternykh, L. N.; Temerov, V. L.; Chu, C. W. Giant magnetoelectric effect in $\text{HoAl}_3(\text{BO}_3)_4$. *Phys. Rev. B: Condens. Matter Mater. Phys.* **2011**, *83*, 180417.

- (6) Hong, H.Y.-P.; Dwight, K. Crystal structure and fluorescence lifetime of $\text{NdAl}_3(\text{BO}_3)_4$, a promising laser material. *Mater. Res. Bull.* **1974**, *9*, 1661–1665.

- (7) Dobretsova, E. A.; Borovikova, E.Yu.; Boldyrev, K. N.; Kurazhkovskaya, V. S.; Leonyuk, N. I. IR spectroscopy of rare-earth aluminum borates $\text{RAl}_3(\text{BO}_3)_4$ (R = Y, Pr–Yb). *Opt. Spectrosc.* **2014**, *116*, 85–92.

- (8) Kokh, A. E.; Kuznetsov, A. B.; Pestryakov, E. V.; Maillard, A.; Maillard, R.; Jobard, C.; Kononova, N. G.; Shevchenko, V. S.; Kragzhda, A. A.; Uralbekov, B.; Kokh, K. A. Growth of the complex borates $\text{Y}_x\text{R}_y\text{Sc}_{2+z}(\text{BO}_3)_4$ (R = Nd, Pr, $x + y + z = 2$) with huntite structure. *Cryst. Res. Technol.* **2017**, *52*, 1600371.

- (9) Wang, G.; Gallagher, H. G.; Han, T. P. J.; Henderson, B. The growth and optical assessment of Cr^{3+} -doped $\text{RX}(\text{BO}_3)_4$ crystals with R = Y, Gd; X = Al, Sc. *J. Cryst. Growth* **1996**, *163* (3), 272–278.

- (10) Krylov, A. S.; Sofronova, S. N.; Gudim, I. A.; Krylova, S. N.; Kumar, R.; Vtyurin, A. N. Manifestation of magnetoelastic interactions in Raman spectra of $\text{Ho}_x\text{Nd}_{1-x}\text{Fe}_3(\text{BO}_3)_4$ crystals. *J. Adv. Dielectr.* **2018**, *8* (2), 1850011.

- (11) Krylov, A.; Moshkina, E.; Sofronova, S.; Gudim, I.; Temerov, V.; Vtyurin, A. Low-temperature features of Raman spectra below magnetic transitions in multiferroic $\text{Ho}_{1-x}\text{Nd}_x\text{Fe}_3(\text{BO}_3)_4$ and $\text{Sm}_{1-y}\text{La}_y\text{Fe}_3(\text{BO}_3)_4$ single crystals. *Ferroelectrics* **2017**, *509* (1), 92–96.

- (12) Krylov, A. S.; Sofronova, S. N.; Gudim, I. A.; Vtyurin, A. N. Magnetoelastic interactions in Raman spectra of $\text{Ho}_{1-x}\text{Nd}_x\text{Fe}_3(\text{BO}_3)_4$ crystals. *Solid State Commun.* **2013**, *174*, 26–29.

- (13) Krylov, A. S.; Gudim, I. A.; Nemtsev, I.; Krylova, S. N.; Shabanov, A. V.; Krylov, A. A. Raman study of $\text{HoFe}_3(\text{BO}_3)_4$ at simultaneously high pressure and high temperature: p–T phase diagram. *J. Raman Spectrosc.* **2017**, *48*, 1406–1410.

- (14) Moshkina, E.; Gudim, I.; Temerov, V.; Krylov, A. Temperature-dependent absorption lines observation in Raman spectra of $\text{SmFe}_3(\text{BO}_3)_4$ ferroborate. *J. Raman Spectrosc.* **2018**, *49*, 1732–1735.

- (15) Moshkina, E.; Krylov, A.; Sofronova, S.; Gudim, I.; Temerov, V. Crystal Growth and Raman Spectroscopy Study of $\text{Sm}_{1-x}\text{La}_x\text{Fe}_3(\text{BO}_3)_4$ Ferroborates. *Cryst. Growth Des.* **2016**, *16* (12), 6915–6921.

- (16) Eremin, E.; Gudim, I.; Temerov, V.; Smolyakov, D.; Molochev, M. Comparing the magnetic and magnetoelectric properties of the $\text{SmFe}_3(\text{BO}_3)_4$ ferroborate single crystals grown using different solvents. *J. Cryst. Growth* **2019**, *518*, 1–4.

- (17) Hinatsu, Y.; Doi, Y.; Ito, K.; Wakeshima, M.; Alemi, A. Magnetic and calorimetric studies on rare-earth iron borates $\text{LnFe}_3(\text{BO}_3)_4$ (Ln = Y, La–Nd, Sm–Ho). *J. Solid State Chem.* **2003**, *172*, 438–445.

- (18) Popov, A. I.; Plokhov, D. I.; Zvezdin, A. K. Quantum theory of magnetoelectricity in rare-earth multiferroics: Nd, Sm and Eu ferroborates. *Phys. Rev. B: Condens. Matter Mater. Phys.* **2013**, *87*, 024413.

- (19) Chaudhury, R. P.; Yen, F.; Lorenz, B.; Sun, Y. Y.; Bezmaternykh, L. N.; Temerov, V. L.; Chu, C. W. Magnetoelectric effect and spontaneous polarization in $\text{HoFe}_3(\text{BO}_3)_4$ and $\text{Ho}_{0.5}\text{Nd}_{0.5}\text{Fe}_3(\text{BO}_3)_4$. *Phys. Rev. B: Condens. Matter Mater. Phys.* **2009**, *80*, 104424.

- (20) Bruker AXS TOPAS V4: User's Manual; General profile and structure analysis software for powder diffraction data; Bruker AXS: Karlsruhe, Germany. 2008.

- (21) Klimin, S. A.; Fausti, D.; Meetsma, A.; Bezmaternykh, L. N.; Van Loosdrecht, P. H. M.; Palstra, T. T. M. Evidence for differentiation in the iron-helicoidal chain in $\text{GdFe}_3(\text{BO}_3)_4$. *Acta Crystallogr., Sect. B: Struct. Sci.* **2005**, *61* (5), 481–485.

- (22) Krylov, A. S.; Kolesnikova, E. M.; Isaenko, L. I.; Krylova, S. N.; Vtyurin, A. N. Measurement of Raman-scattering spectra of

Rb₂KMoO₃F₃ crystal: Evidence for controllable disorder in the lattice structure. *Cryst. Growth Des.* **2014**, *14*, 923.

(23) Taniguchi, H.; Itoh, M.; Fu, D. Raman scattering study of the soft mode in Pb(Mg_{1/3}Nb_{2/3})O₃. *J. Raman Spectrosc.* **2011**, *42* (4), 706–714.

(24) Kresse, G.; Joubert, D. From ultrasoft pseudopotentials to the projector augmented-wave method. *Phys. Rev. B: Condens. Matter Mater. Phys.* **1999**, *59*, 1758.

(25) Kresse, G.; Furthmüller, J. Efficient iterative schemes for ab initio total-energy calculations using a plane-wave basis set. *Phys. Rev. B: Condens. Matter Mater. Phys.* **1996**, *54*, 11169.

(26) Perdew, J. P.; Burke, K.; Ernzerhof, M. Generalized Gradient Approximation Made Simple. *Phys. Rev. Lett.* **1996**, *77*, 3865.

(27) Monkhorst, H. J.; Pack, J. D. Special points for Brillouin-zone integrations. *Phys. Rev. B* **1976**, *13*, 5188.

(28) Dudarev, S. L.; Botton, G. A.; Savrasov, S. Y.; Humphreys, C. J.; Sutton, A. P. Electron-energy-loss spectra and the structural stability of nickel oxide: An LSDA+U study. *Phys. Rev. B: Condens. Matter Mater. Phys.* **1998**, *57*, 1505.

(29) Stanislavchuk, T. N.; Chukalina, E. P.; Popova, M. N.; Bezmaternykh, L. N.; Gudim, I. A. Investigation of the iron borates DyFe₃(BO₃)₄ and HoFe₃(BO₃)₄ by the method of Er³⁺ spectroscopic probe. *Phys. Lett. A* **2007**, *368* (5), 408–411.

(30) Zinenko, V. I.; Pavlovskii, M. S.; Krylov, A. S.; Gudim, I. A.; Eremin, E. V. Vibrational spectra and elastic, piezoelectric, and magnetoelectric properties of HoFe₃(BO₃)₄ and HoAl₃(BO₃)₄ crystals. *J. Exp. Theor. Phys.* **2013**, *117*, 1032–1041.